A novel multi-detection technique for three-dimensional reciprocal-space mapping in grazing-incidence X-ray diffraction

M. Schmidbauer,[a]* P. Schäfer,[b] S. Besedin,[c] D. Grigoriev,[d] R. Köhler[b] and M. Hanke[e]

[a]Leibniz Institut für Kristallzüchtung, Max-Born-Strasse 2, D-12489 Berlin, Germany, [b]Institut für Physik, Humboldt-Universität zu Berlin, Newtonstrasse 15, D-12489 Berlin, Germany, [c]Shubnikov Institute of Crystallography, Russian Academy of Science, Moscow 119333, Russian Federation, [d]Universität Karlsruhe (TH), Fakultät für Physik, Postfach 6980, D-76128 Karlsruhe, Germany, and [e]Martin-Luther-Universität Halle-Wittenberg, Institut für Physik, Hoher Weg 8, D-06120 Halle/Saale, Germany. E-mail: schmidbauer@ikz-berlin.de

A new scattering technique in grazing-incidence X-ray diffraction geometry is described which enables three-dimensional mapping of reciprocal space by a single rocking scan of the sample. This is achieved by using a two-dimensional detector. The new set-up is discussed in terms of angular resolution and dynamic range of scattered intensity. As an example the diffuse scattering from a strained multilayer of self-assembled (In,Ga)As quantum dots grown on GaAs substrate is presented.

Keywords: grazing-incidence X-ray diffraction; three-dimensional reciprocal-space mapping; multi-detection; InGaAs quantum dots.

1. Introduction

X-ray scattering is a powerful and well established tool for the non-destructive structural characterization of matter. Among a variety of different techniques, high-resolution X-ray diffraction is particularly suitable for the investigation of highly perfect crystalline structures. One of the main benefits is the high angular resolution of just a few seconds of arc which makes X-rays sensitive to very small changes of lattice parameters.

There are specific advantages in the investigation of thin layers and multilayered structures (Pietsch *et al.*, 2004). The penetration depth of the X-rays can be tuned from a few nanometers up to a couple of micrometers. This range is well adapted to typical thicknesses of semiconductor epitaxial layer systems. Moreover, thanks to spatial coherence lengths of typically a few micrometers, information on electron density fluctuations on a large scope of length scales can be obtained. This so-called mesoscopic regime, ranging from a few nanometers up to some micrometers, plays a very important role in the self-organized formation of semiconductor nanostructures and has attracted overwhelming interest in the past years (*e.g.* Bimberg *et al.*, 1998; Shchukin *et al.*, 2003). In particular, semiconductor quantum dots and wires have been extensively investigated, and X-ray scattering techniques have proved to be extremely suitable for a non-destructive characterization (Schmidbauer, 2004; Stangl *et al.*, 2004).

The investigation of nanostructures requires the employment of sophisticated experimental set-ups. On the one hand, owing to the small scattering volumes, highly intense synchrotron radiation is a mandatory prerequisite. On the other hand, in many cases ultra-high resolution is not necessary. However, the small size, particular shape and inhomogeneous strain of nanostructures lead to a characteristic distribution of diffuse intensity which has to be recorded in all three dimensions in reciprocal space.

When monochromatic X-rays are used, reciprocal space can be probed by choosing appropriate directions of the incident and scattered beams. Precise measurements of both the incident angles and the scattering angles require a triple-crystal set-up, the principal advantage of which is the ability to map reciprocal space with extremely high resolution. A well defined direction of the incidence wavevector is guaranteed since a collimated X-ray beam is used. The direction of the scattered beam is then determined by a crystal analyzer or, when only medium resolution is required, by a collimating slit system. The actual choice depends on the scattering geometry and, therefore, on the required resolution, dynamical range and area of interest in reciprocal space. However, the corresponding large data collection times represent a serious disadvantage and make this technique unfeasible for recording the three-dimensional intensity distribution in reciprocal space. The scanning of, for example, $100 \times 100 \times 100 = 10^6$ data points, where each point is recorded in a time

of only 1 s, requires a total data collection time of several hundreds of hours, even if highly brilliant synchrotron radiation is employed.

Three-dimensional reciprocal-space mapping can only be realised by applying sophisticated multi-detection techniques, where position-sensitive detectors are used to analyze the diffuse scattering. This technique has been successfully applied for grazing-incidence small-angle scattering (GISAXS) (*e.g.* Levine *et al.*, 1989; Naudon & Thiaudiere, 1997; Schmidbauer *et al.*, 1998).

The diffuse scattering in GISAXS is collected in the vicinity of the specularly reflected beam, which makes this technique particularly sensitive to the surface and near-surface regime of thin layers. Density fluctuations are probed on the mesoscopic length scale while there is no sensitivity to lattice strains. In order to combine both surface sensitivity and strain sensitivity the diffuse scattering can be probed in the vicinity of a non-zero in-plane reciprocal lattice point. With this technique, which is called grazing-incidence X-ray diffraction (GIXD), the incident and scattered beams make very small 'grazing' angles with respect to the sample surface. Often, a linear position-sensitive detector is used to probe the intensity distribution as a function of the exit angle to the surface, while the in-plane intensity distribution is recorded by rotating the sample and the detector. This means that three-dimensional mapping is possible, but it requires the independent movement of two different axes which makes this technique rather time-consuming. Typical data collection times are in the regime of 20 h and more.

The use of area detectors opens up new possibilities in grazing-incidence diffraction. For example, Schlepütz *et al.* (2005) have employed a two-dimensional pixel detector to probe the intensity distribution along crystal truncation rods (CTRs) in grazing-incidence scattering geometry. CTRs reveal information about the surface morphology and atomic structure as compared with the bulk (*e.g.* Feidenhans'l, 1989). Since CTRs are one-dimensional features, these experiments do not require three-dimensional mapping of reciprocal space. Area detectors have also been used for grazing-incidence X-ray scattering from Langmuir–Blodgett films and for X-ray liquid surface scattering (*e.g.* Foran *et al.*, 1996; Fontaine *et al.*, 2004). In these experiments the configuration is optimized to measure very low signals, while a rather limited angular resolution and dynamic range have to be taken into account. Therefore, a true three-dimensional mapping of reciprocal space is, at least in most cases, not intended.

In this paper we describe a novel multi-detection technique for recording the diffuse scattering in GIXD geometry. Its particular advantage lies in the fact that three-dimensional reciprocal-space mapping can be performed by a single rocking scan of the sample. The use of an area detector drastically reduces the data collection time and enables three-dimensional mapping of reciprocal space around an in-plane reciprocal lattice point. A specific advantage is the tunability of the in-plane resolution and angular range which can thus be adapted to the requirement of a particular sample.

The paper is organized as follows. After a short introduction into the basic principle of multi-detection techniques (§2) we briefly review well known multi-detection techniques for GISAXS and co-planar wide-angle scattering (§3). This is followed by an introduction and discussion of our novel technique. In §4 the experimental set-up at the BW2 wiggler beamline at HASYLAB/DESY is described. In §5 a selected sample consisting of multilayered strained (In,Ga)As quantum dots embedded in a GaAs matrix is presented. Finally, in §6, we discuss the particular advantages of our new set-up in view of resolution, angular range and applicability to mesoscopic systems.

2. Multi-detection techniques for reciprocal-space mapping – an introduction

The scattering vector $\mathbf{Q}$ is related to the wavevectors of incident ($\mathbf{k}_i$) and scattered ($\mathbf{k}_f$) waves according to the equation

$$\mathbf{Q} = \mathbf{k}_f - \mathbf{k}_i, \tag{1}$$

where $k_i = k_f = 2\pi/\lambda$ with λ representing the X-ray wavelength. We can express the components of the scattering vector as

$$\begin{aligned} Q_x &= (2\pi/\lambda)\big[\cos\alpha_f \cos(2\theta - \omega) - \cos\alpha_i \cos\omega\big], \\ Q_y &= (2\pi/\lambda)\big[\cos\alpha_f \sin(2\theta - \omega) + \cos\alpha_i \sin\omega\big], \\ Q_z &= (2\pi/\lambda)(\sin\alpha_f + \sin\alpha_i). \end{aligned} \tag{2}$$

Here $\alpha_{i,f}$ are the glancing angles of incidence and exit with respect to the sample surface (xy plane). ω is the in-plane angle of the X-ray beam with respect to the x-axis, and 2θ is the in-plane scattering angle (Fig. 1). Note that we have defined the incident and scattering angles as commonly used in grazing-incidence diffraction.

The difficulty of long data collection times that arises when a triple-axis diffractometer is used can be overcome by utilizing modern area detectors or, at least, a linear position-sensitive detector (PSD). This idea was first suggested by Mathieson (1982), and its application to epitaxial materials was discussed by Lee *et al.* (1995). For a sufficiently small spot size at the sample and sufficiently good spatial resolution an area detector offers parallel determination of the scattering angles α_f and 2θ (see Fig. 2). This multi-detection technique
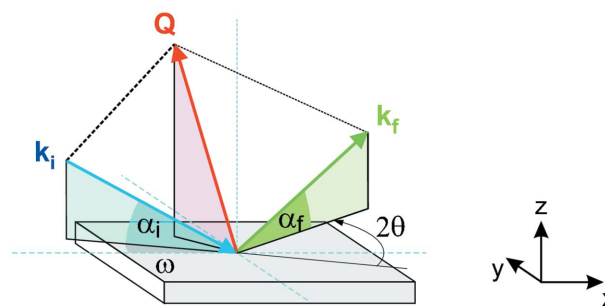

Figure 1
Definition of scattering vector $\mathbf{Q}$ by the glancing angles α_i, α_f and the in-plane angles ω, 2θ.
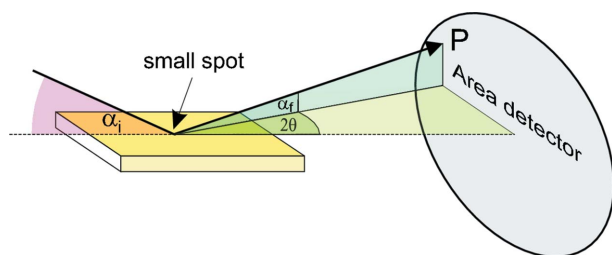
Figure 2
Principle of multi-detection in an X-ray scattering experiment using a small spot size at the sample. For sufficiently good spatial resolution, each point P on an area detector corresponds to unique values of α_f and 2θ. The diffuse scattering at different values of these angles is probed in a parallel measurement without scanning the sample (fixed α_i and ω). The angular resolution depends on the spot size at the sample, the spatial resolution of the detector and the distance between detector and sample.

substantially reduces the data acquisition time, and a two-dimensional mapping (using a linear PSD) or a three-dimensional mapping (using an area detector) of reciprocal space can then be performed in a very short time, similar to that for a one-dimensional rocking scan.

For a spot size of $\sim 200\ \mu$m and a distance between the sample and the detector of about 1000 mm, the angular resolution of the diffracted beam is of order $\delta(2\theta) = 2 \times 10^{-4}$ rad. This intermediate resolution, though definitely worse than the high resolution provided by a crystal analyzer where $\delta(2\theta) = 2 \times 10^{-5}$ rad, often turns out to be sufficient for the analysis of diffuse scattering.

3. Three-dimensional reciprocal-space mapping for different scattering geometries

In this section we will describe the use of a two-dimensional detector for three-dimensional mapping of reciprocal space in different scattering geometries. We summarize first the well known cases of coplanar wide-angle scattering and grazing-incidence small-angle scattering. Then we will introduce and discuss a new technique of three-dimensional reciprocal-space mapping in GIXD geometry.

3.1. Coplanar wide-angle X-ray scattering (CWAXS)

With CWAXS, coplanar reciprocal lattice points are probed. For these points one can always choose a scattering geometry where the X-ray beam impinges the surface under a comparatively large incident angle α_i, and a small spot of illuminating X-rays can be created on the sample. This finally leads to a small effective size of the scattered beam. Therefore, each point on the two-dimensional detector can be non-ambiguously assigned to a unique pair of scattering angles (2θ, α_f) and thus, provided that the incoming beam is well collimated and monochromatic, to a well defined scattering vector. Three-dimensional reciprocal-space mapping is then usually performed by a single rocking scan (α_i scan) of the sample at fixed detector, or, if a larger range of scattering angles is needed, by a combined 1:2 scan of sample and detector.

At a given distance D between detector and sample, and a vertical and horizontal beam size of p_1 and p_2, respectively,

Table 1
Calculated angular resolution for different scattering techniques.

The following parameters are used: $\lambda = 0.15$ nm, $D = 1000$ mm, $L = 10$ mm, $T = 30$ mm; $\alpha_i = \alpha_f = 0.5°$ (GIXD, GISAXS); $\alpha_i = \alpha_f = 30°$ (CWAXS); $\omega = 22.5°$, $2\theta = 45°$ (GIXD); $2\theta = 1°$ (GISAXS, CWAXS); $p_1 = p_2 = 200\ \mu$m (GISAXS, CWAXS); $p_1 = 200\ \mu$m, $p_2 = 1$ mm, $s_2 = 0.5$ mm (GIXD).

Technique	$\delta\omega$ (rad)	$\delta\alpha_i$ (rad)	$\delta(2\theta)$ (rad)	$\delta\alpha_f$ (rad)
CWAXS	2×10^{-4}	1×10^{-4}	2×10^{-4}	2×10^{-4}
GISAXS	1×10^{-4}	2×10^{-4}	4×10^{-4}	9×10^{-5}
GIXD	1×10^{-4}	5×10^{-4}	5×10^{-4}	6×10^{-5}

the resolution in angular space can be estimated as (see Fig. 3)

$$\delta\alpha_f = \frac{\sin\alpha_f}{\sin\alpha_i}(p_1/D),$$
$$\delta(2\theta) = p_2/D. \tag{3}$$

The validity of (3) requires small in-plane scattering angles 2θ. In addition, we have to neglect that the X-ray beam may strongly penetrate into the sample. Note that the in-plane resolution $\delta(2\theta)$ is independent of the scattering angles. On the other hand, the out-of-plane resolution $\delta\alpha_f$ is very good for large incidence angles α_i and small scattering angles α_f. This is the case for coplanar asymmetrical reflections with glancing exit angle. A large vertical beam size p_1 can be used when asymmetrical reflections are under investigation. For small values of α_f the detector is almost perpendicular to the surface. It is therefore very convenient to map reciprocal space by performing a single rocking scan of the sample. Typical values for the angular resolution are given in Table 1.
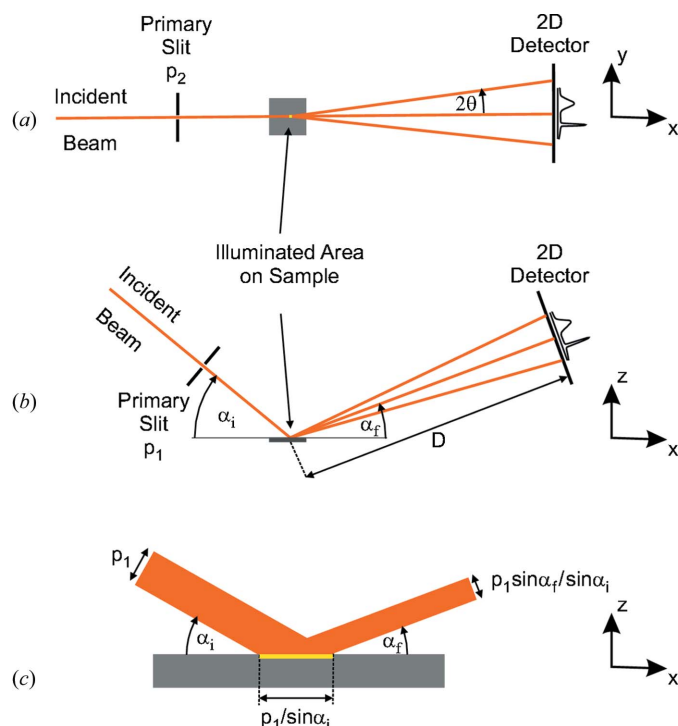

Figure 3
In-plane (a) and out-of-plane (b) scattering geometry in coplanar wide-angle diffraction. (c) Vertical beam size of scattered beam as a function of p_1, α_i and α_f.
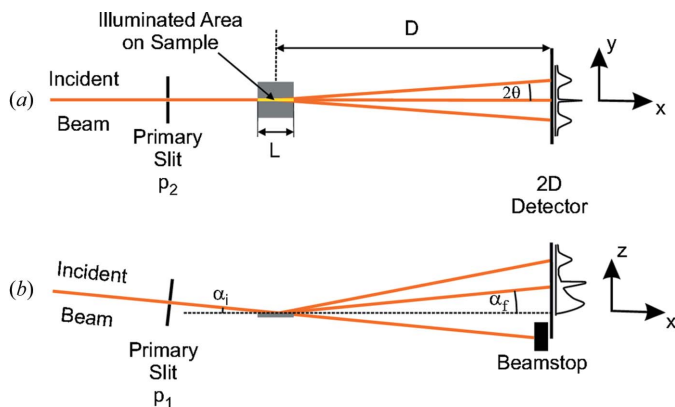
Figure 4
In-plane (*a*) and out-of-plane (*b*) scattering geometry for GISAXS.

3.2. GISAXS

For GISAXS the incident beam impinges the surface under very small 'grazing' angles. The diffuse scattering is then analyzed in the vicinity of the specularly reflected beam. Small primary slits p_1 and p_2 are commonly used; however, owing to the small incident angle α_i the incident beam creates a narrow linear footprint on the sample (Fig. 4). Since only small scattering angles (α_f, 2θ) are probed, this linear footprint on the sample translates into a slightly broadened but still narrow reflected beam, which produces a small spot on the detector. A three-dimensional mapping of reciprocal space is then performed by a full azimuthal rotation of the sample around the z-axis keeping the angle of incidence α_i constant.

The in-plane angular resolution can be expressed as

$$\delta(2\theta) = \Delta/D, \tag{4}$$

where Δ is the in-plane size of the scattered beam,

$$\Delta = L\sin(2\theta) + p_2\cos(2\theta) \simeq L\,2\theta + p_2. \tag{5}$$

Here, L is the length of the illuminated footprint on the sample. Note that the in-plane angular resolution depends on the in-plane scattering angle 2θ.

In the out-of-plane direction the angular resolution is given by

$$\delta\alpha_f = (L/D)\sin\alpha_f \simeq (L/D)\alpha_f = \delta z/D, \tag{6}$$

with the out-of-plane dimension, δz, of the scattered beam. For $L = 10$ mm and $\alpha_f = 0.5°$ we obtain $\delta z = 90$ µm, which is close to the spatial resolution of our detector (see §4). Typical values of the angular resolution are listed in Table 1.

3.3. GIXD

3.3.1. Basic principle. Similar to GISAXS the incident beam creates a long footprint on the sample. However, in GIXD geometry the diffuse scattering is probed in the proximity of a Bragg reflection. The large in-plane scattering angle 2θ transforms the footprint on the sample into a broad scattered beam which creates a broad horizontal spot on the two-dimensional detector. This can be seen in equation (5) where, for example, $p_2 = 0.2$ mm, $L = 10$ mm and $2\theta = 45°$ leads
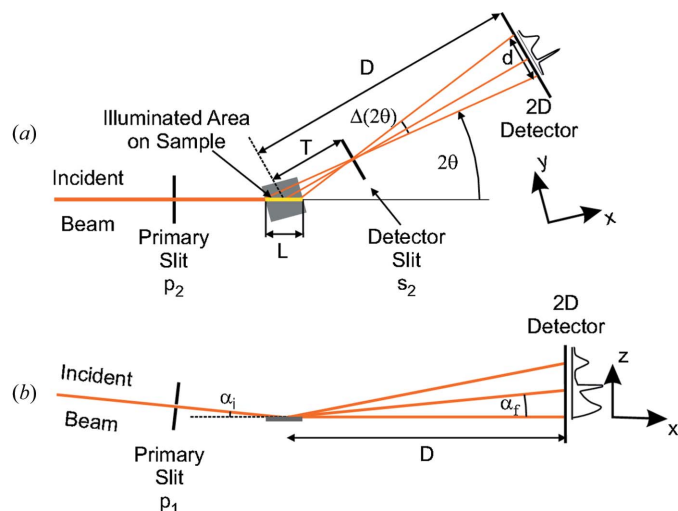

Figure 5
In-plane (*a*) and out-of-plane (*b*) scattering geometry for GIXD.

to $\Delta = 7$ mm. Therefore, the principle as utilized for GISAXS cannot be applied to this scattering geometry, even if the horizontal size p_2 of the incidence beam is strongly reduced.

Therefore, often a linear PSD oriented perpendicular to the sample surface along with a collimating slit system (*e.g.* Soller slits) in the horizontal direction is used. Alternatively, if higher resolution is required, a crystal analyzer probing the horizontal component of the scattering vector is utilized. In both cases, three-dimensional mapping is achieved by the time-consuming movement of two independent axes, ω and 2θ.

The experimental set-up as sketched in Fig. 5 represents a way out of this dilemma. The sample is illuminated at glancing angle α_i such that a broad stripe on the sample surface is illuminated. Directly behind the sample, a small horizontal slit s_2 is placed. Thus, each point on the two-dimensional detector corresponds to unique values of α_f and 2θ. Therefore, a three-dimensional mapping of reciprocal space can be performed by a single scan of the sample.

3.3.2. Resolution. The angular resolution of the in-plane scattering angle is determined by

$$\delta(2\theta) = s_2/(D - T), \tag{7}$$

where T is the distance between sample and detector slit. Here, it should be stressed that the angular resolution is independent of the incident slit p_2, *i.e.* the horizontal beam size. However, the scattered intensity at a fixed pixel of the detector linearly increases with p_2 while the detector slit s_2 is kept unchanged. Therefore the horizontal slit p_2 should be opened as much as possible in order to obtain maximum intensity.

We can adapt the values for angular resolution $\delta(2\theta)$ to the particular requirements of a given sample by changing the slit size s_2. We recommend that the slit s_2 is always larger than the spatial resolution of the detector which is, in our case, about 60 µm. By applying, for example, $s_2 = 0.5$ mm, $D = 1000$ mm, $T = 100$ mm, $L = 10$ mm and $2\theta = 45°$, a typical value of $\delta(2\theta) = 0.032°$ is achieved.

The out-of-plane angular resolution is given by

$$\delta\alpha_{\mathrm{f}} = \frac{p_2}{D}\frac{\sin\alpha_{\mathrm{f}}}{\sin 2\theta} = \frac{\delta z}{D}. \qquad (8)$$

The out-of-plane-dimension δz of the diffracted beam is very small. Therefore, the effective out-of-plane angular resolution is determined by the spatial resolution (pixel size) of the two-dimensional detector which in our case is $\delta z = 60\ \mu$m (see §4.2). Typical values of the angular resolution are given in Table 1.

3.3.3. Accessible angular range. When assuming that p_2 (typically 1 mm) is significantly smaller than L (typically 10 mm), the in-plane angular range $\Delta(2\theta)$ is given by

$$\Delta(2\theta) = \frac{\Delta}{T} \simeq \frac{L\sin(2\theta)}{T}, \qquad (9)$$

where Δ is the in-plane size of the scattered beam, 2θ is the in-plane scattering angle and L is the length of the illuminated area on the sample (see Fig. 5). According to this relationship the angular range $\Delta(2\theta)$ can be tuned to meet the requirements of a particular sample. For $T = 100$ mm, $L = 10$ mm and $2\theta = 45°$, a value of $\Delta(2\theta) = 0.07$ rad $= 4°$ is obtained. The corresponding spatial spread of diffuse scattering on the two-dimensional detector is $d = \Delta(2\theta)(D - T) = 63$ mm, which fits well to the spatial range of the used APEX 2 CCD detector (see §4).

If the sample need not be placed into a special environment (e.g. cryostat or oven), the distance T can be further reduced to reach very small values. The case of small values of T is highly desirable since then angular information is strongly disentangled from the spatial position on the sample. For small values of T the angular range is limited by the spatial acceptance D_{det} of the detector,

$$\Delta(2\theta) = D_{\mathrm{det}}/D. \qquad (10)$$

The angular range can thus be increased by reducing the distance between detector and sample, and with, for example, $D_{\mathrm{det}} = 62$ mm and $D = 500$ mm we obtain $\Delta(2\theta) = 0.12$ rad $= 7.1°$. However, the angular resolution will be reduced according to equations (7) and (8).

4. Experimental set-up

4.1. Diffractometer

Experiments were performed at BW2 wiggler beamline at HASYLAB/DESY. Monochromatic X-rays with a wavelength of $\lambda = 1.5$ Å were used. The sample was mounted on a four-circle diffractometer in a vertical scattering geometry. A large detector arm was installed in order to carry a heavy CCD detector. It is worth mentioning that the diffractometer can be used for all three scattering geometries, i.e. GIXD, GISAXS and CWAXS. For GISAXS and GIXD the sample is mounted in a vertical position, with the surface normal pointing in the horizontal direction. The angle of incidence α_{i} is set by azimuthally rotating the entire diffractometer. In CWAXS geometry the sample is mounted in a horizontal position. A photograph of the experimental set-up is shown in Fig. 6.
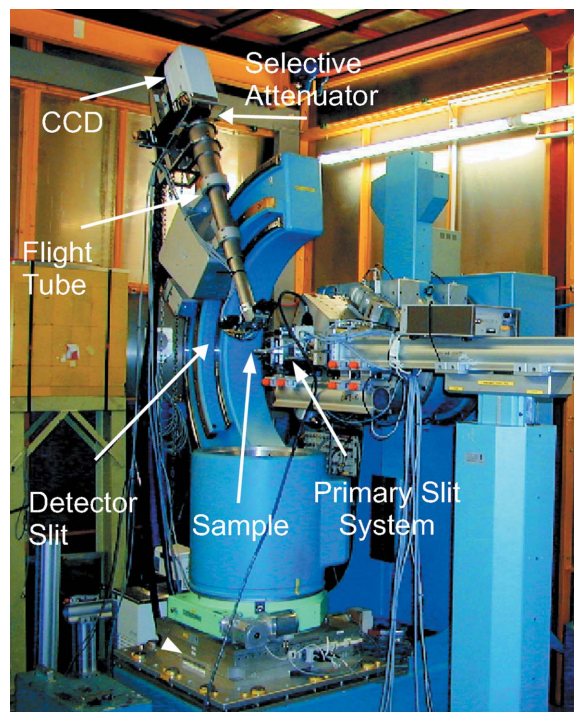

Figure 6
Experimental set-up at BW2 beamline (HASYLAB/DESY).

4.2. CCD detector

APEX 2 is a large-format two-dimensional CCD detector (BRUKER AXS), where the size of the scintillator coincides with the size of the CCD chip, i.e. the fiber optics consist of a 1:1 faceplate (more than 70% transmittivity) instead of a magnifying taper (less than 10% transmittivity). The detector is operating in a 1024×1024 pixel mode with an effective pixel size of 60 μm, yielding a spatial range of about 62 mm $\times$ 62 mm. The maximum counts per pixel is $N = 2^{16} = 65536$ with a dark current ($T = 240$ K) of about 1.5 ADU pixel^{-1} and a readout noise (1 s readout time) of 1.3 ADU pixel^{-1} (ADU = analogue to digital unit). Four low-noise output amplifiers are used to read out the CCD chip.

4.3. Selective attenuators

In order to avoid saturation or even damage of the detector, the scattered X-ray beam has to be attenuated if it is too intense. It is very often the case that strong intensity is concentrated in a small spot (e.g. diffraction from a perfect crystalline substrate) or a narrow rod (e.g. crystal truncation rod). Then selective attenuators, e.g. a small metal disc (see Fig. 7a) or a narrow metal wire, can be directly placed in front of the detector.

4.4. Collimation, slit system and beam size

The basic optical elements of BW2 beamline consist of a plane Au-coated pre-mirror, a $(+n, -n)$ Si(111) double-crystal monochromator and a second curved Au-coated mirror located behind the monochromator. The X-ray beam is focused vertically and horizontally onto the sample. Hori-

zontal focusing is achieved by a sagittally bent second monochromator crystal while the second bent mirror focuses the monochromatic beam in the vertical direction. According to the divergent wiggler source, along with 3:1 horizontal focusing our set-up leads to a comparatively large beam divergence at the sample position (up to several mrad for the full beam) and, thus, to a rather broad X-ray spot size on the detector. This holds particularly for the horizontal beam size. Therefore, in order to reduce horizontal divergence, additional slits after the monochromator can be employed. Typical values for the incident divergences are $\delta\alpha_i = 2 \times 10^{-4}$, $\delta\omega = 1 \times 10^{-4}$ (GISAXS) and $\delta\alpha_i = 5 \times 10^{-4}$, $\delta\omega = 1 \times 10^{-4}$ (GIXD) (see also Table 1).

The need to probe the diffuse scattering over a large dynamic range close to strong coherent beams (e.g. Bragg reflections or the specular beam) requires a very 'clean' incident beam profile. On the other hand, a small spot size of typically 50–200 µm at the sample is necessary. Therefore, high-quality slits have to be used, and a set-up consisting of sequential slits is most advantageous. The first slits ('primary slits') act as a beam size limitation while the second slits ('anti-scattering slits') suppress the scattering from the primary slits.

The high efficiency of such a double-slit system is demonstrated in Fig. 7(a). Here, the profile of the incident beam is displayed as measured on the CCD detector without using anti-scattering slits. The central part of the strong primary beam has been attenuated by a lead beam-stop (5 mm diameter). In the close vicinity of the primary beam, strong features arising from scattering from the primary slits are visible. As a comparison, Fig. 7(b) shows the primary beam profile when using anti-scattering slits. As can be clearly seen, all artificial features owing to slit scattering are now strongly suppressed.

The primary slits were chosen as $p_1 = p_2 = 200$ µm, resulting in corresponding vertical and horizontal peak widths at the CCD detector of about 270 µm and 400 µm, respectively. This increase of the peak widths is caused by the finite vertical and horizontal divergence of the primary beam. Respective linear horizontal and vertical sections through the center of the primary beam are presented in Figs. 7(c) and 7(d). From these sections it is proven that the primary beam is 'clean', i.e. it does not show any artifacts in the tails of the peak profile. Note also that the dynamic range of almost five orders of magnitude is given by the dynamic range of the CCD detector.

5. Experimental results

5.1. Test sample

In order to test our method we have chosen a multilayer of self-assembled semiconductor quantum dots (QDs). There is considerable interest in such systems owing to possible device applications in, for example, optoelectronics, whereby the QD size, shape, positions, composition and strain state act as key design parameters.

The QD multilayer structure consists of 16.5 periods of ten monolayers (ML) $In_{0.40}Ga_{0.60}As$ QDs and 120 ML GaAs spacers that are grown by molecular beam epitaxy on a GaAs (411)B substrate. The last layer of the QDs was left exposed for topographic atomic force microscopy (AFM) imaging under ambient conditions. The AFM micrograph (Fig. 8) shows dots with a base width of about 30 nm and a corresponding height of 5 nm, and the QDs form an almost perfect three-dimensional lattice. Further information on this and similar samples can be found by Schmidbauer et al. (2006) and Springholz et al. (1998).

The choice of this particular sample relies on specific reasons. (i) Owing to the small volume of these tiny objects, which are epitaxially grown on a thick substrate, grazing-incidence diffraction is a mandatory tool in order to enhance the scattering signal from the QDs as compared with that of the bulk crystal. (ii) The small strained quantum dots lead to extended diffuse intensity which is widely distributed in reciprocal space. (iii) Very small strained objects grown on a perfect substrate provide a large dynamic range of scattered intensity. (iv) Besides the diffuse scattering from the QDs, there is always a very narrow
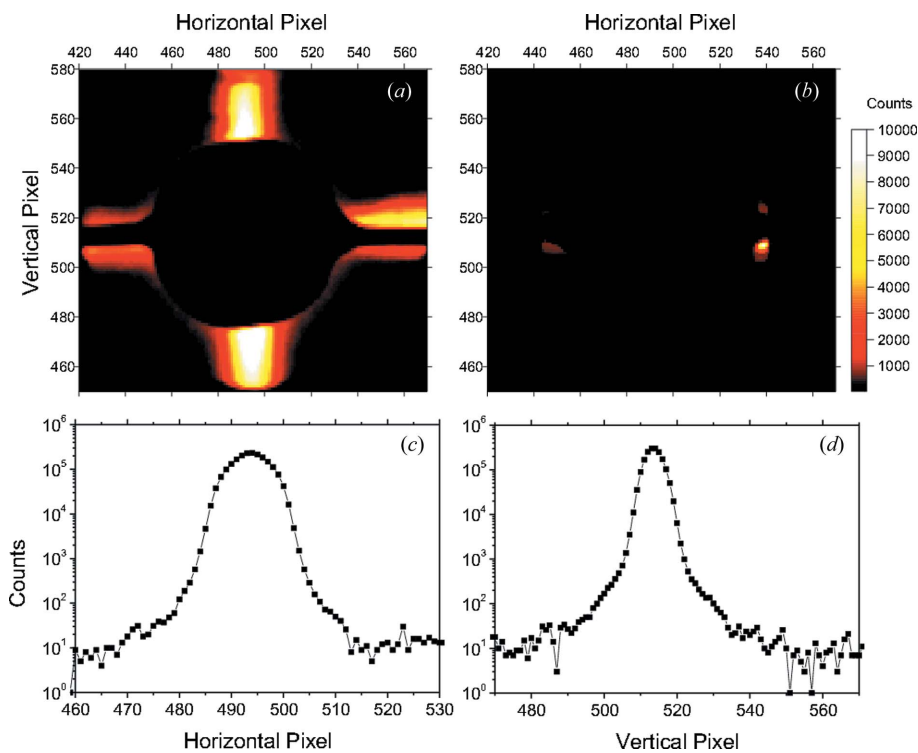

Figure 7
Profile of the narrow primary beam measured on a CCD detector, (a) without anti-scattering slits using a beam-stop and (b) with anti-scattering slit using a beam-stop. (c) Horizontal and (d) vertical sections through the center of the primary beam as shown in (b) without using the beam-stop.
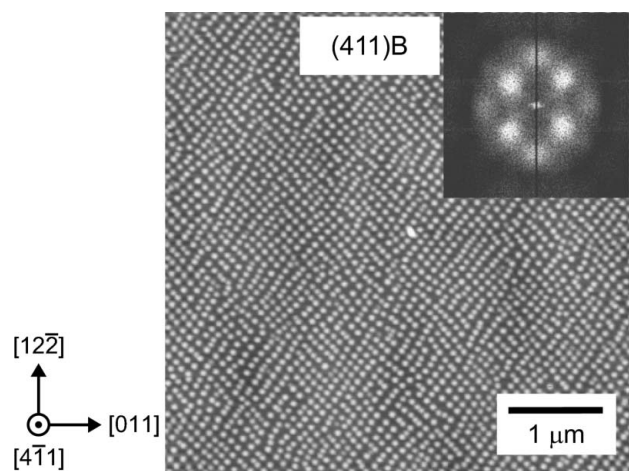
Figure 8
AFM micrograph of the surface of a multilayered sample of InGaAs QDs grown on GaAs (411)B. The inset shows a Fourier transform of the height profile.

Figure 9
CCD frame measured in GIXD geometry for a multilayered InGaAs QD sample collected in the vicinity of the GaAs 022 substrate reflection (α_i = 0.5°). T = 30 mm, D = 1000 mm, s_2 = 1 mm. Besides the substrate reflection (S), the intensity distribution is caused by the sample surface and interfaces (CTR), the inhomogeneous strain distribution (W) and the spatial ordering (P) of the QDs.

substrate Bragg reflection which can be used to check the resolution in reciprocal space. (v) The almost perfect three-dimensional arrangement of the QDs in the sample leads to a corresponding three-dimensional lattice of narrow satellite peaks which appears in close vicinity of a reciprocal lattice point. Accurate analysis of the spatial arrangement of the QDs thus requires a three-dimensional analysis of diffuse scattering

5.2. Treatment of raw data and data evaluation procedure

A single CCD frame measured close to the 022 in-plane reciprocal lattice point is displayed in Fig. 9. The intensity distribution is rich in detail, caused by the substrate reflection (S), the sample surface and interfaces (CTR), the inhomogeneous strain distribution (W) and the spatial ordering (P) of the QDs.

Reciprocal-space mapping was performed by rotating the sample azimuthally (ω-scan) at a fixed angle of incidence (α_i = 0.5°). The procedure described above leads to a set of different CCD frames where each frame corresponds to a certain incident angle ω. For the actual sample the step width in ω was chosen to be 0.005° with a data acquisition time per point of 30 s. With a total ω range of 2°, 401 data points were collected leading to a total data acquisition time (including time for CCD readout and motor movements) of less than 4 h.

The intensity data are normalized with respect to the signal of an ionization chamber located directly behind the primary slits which measures the flux of the incident beam on the sample. For samples with non-circular symmetry (usually the samples are rectangular with a size of typically 10 mm × 10 mm), the footprint on the sample may change during an ω scan (see *e.g.* Schlepütz *et al.*, 2005). However, since the range of the ω scan and the angular acceptance of the CCD detector usually amounts to some few degrees only, we can neglect this effect in very good approximation.

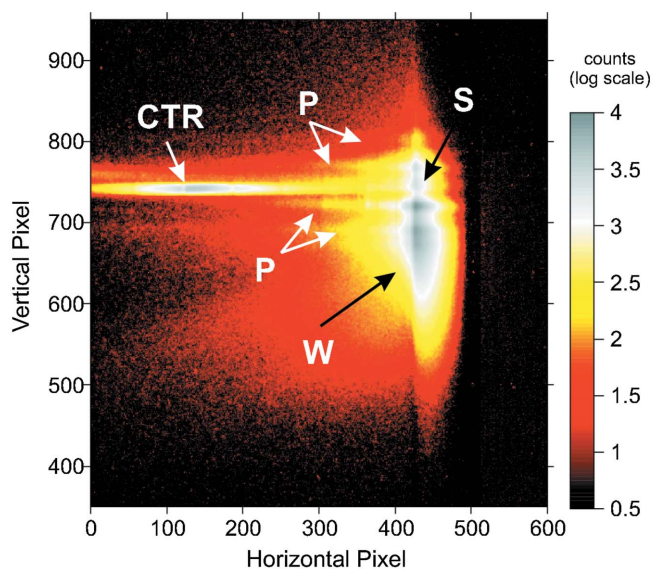The data were further processed by a linear interpolation procedure in that the normalized intensity data were put on a regular grid in three-dimensional reciprocal space. Depending on the number of CCD frames used and the mesh size in reciprocal space, the calculation of a three-dimensional reciprocal-space map from the raw data takes between a couple of minutes up to several hours (on a standard commercial computer).

5.3. Two-dimensional sections of intensity distribution in reciprocal space

Selected two-dimensional sections can be extracted from the three-dimensional intensity distribution in reciprocal space. Fig. 10 exemplarily displays an in-plane two-dimensional reciprocal-space map in the vicinity of the GaAs 022 in-plane reciprocal lattice point (α_i = 0.5°).

The diffuse intensity is widely distributed in reciprocal space. A detailed interpretation is only possible by corresponding X-ray simulations in the framework of the distorted-wave Born approximation (Schmidbauer *et al.*, 2005) or other sophisticated approaches (*e.g.* Kegel *et al.*, 2000). However, the origin of the different features appearing in Fig. 10 can be discussed qualitatively. The extended tail in the radial direction ([011]) is caused by the inhomogeneous strain distribution inside the QDs and the surrounding GaAs matrix. This strain-induced diffuse scattering is superimposed by intensity modulations caused by the finite size and the particular shape of the QDs. Finally, the sharp satellite peaks in the close vicinity of the GaAs 022 substrate reflection are caused by the almost perfect horizontal ordering of the QDs inside the sample. This ordering can be observed at the sample surface (Fig. 8); however, it is also present inside the entire QD stack. From the peak positions in different directions (relative to the substrate reflection) the corresponding distances in real space
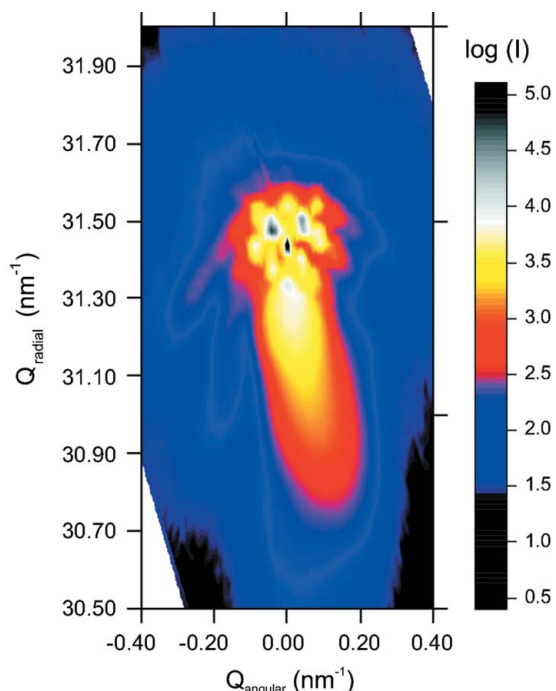
Figure 10
Measured GIXD in-plane reciprocal-space map of an InGaAs quantum dot sample in the vicinity of the 022 reflection. The intensity distribution is shown for $Q_z = Q_{4\bar{1}1} = 0.55$ nm^{-1}, with an integration interval of $\Delta Q_z = 0.19$ nm^{-1} (which corresponds to 80 CCD pixels). The strain-sensitive radial scan direction is collinear with [011] while the angular scan direction is collinear with [12$\bar{2}$].

can be calculated. In addition, the respective correlation lengths can be calculated from the peak widths (Kegel *et al.*, 1999; Stangl *et al.*, 2000). We have to emphasize that the satellite peaks are considerably broader than the sharp substrate reflection proving that the correlation lengths are not resolution-limited.

Although being influenced by strain, the central part of the GIXD intensity pattern close to the substrate reflection can
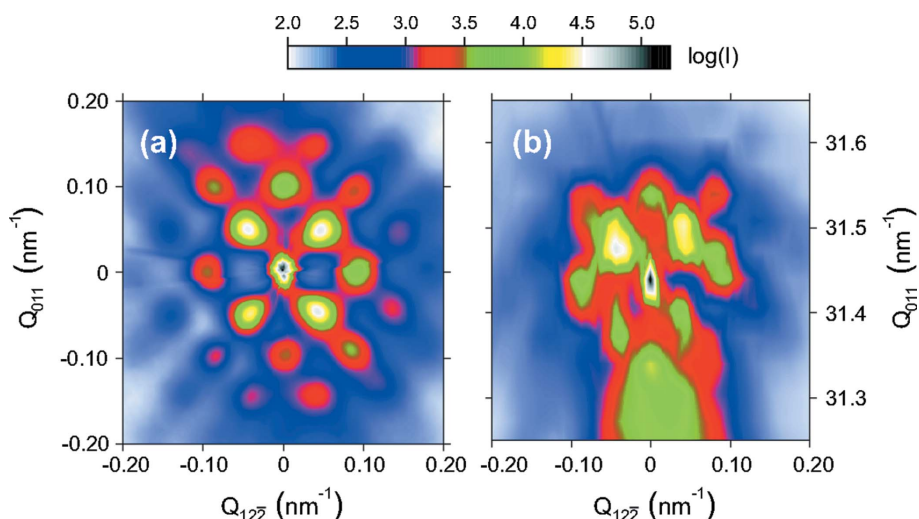

Figure 11
Comparison of satellite peaks in the vicinity of (*a*) 000 (GISAXS) and (*b*) 022 (GIXD).

be compared with corresponding features in the in-plane GISAXS intensity distribution. A comparison is shown in Fig. 11. Here, the resolution conditions chosen in GISAXS (Fig. 11*a*) are slightly better than those chosen in GIXD (Fig. 11*b*). However, all relevant features of diffuse scattering that are visible in GISAXS can be also observed in GIXD.

The overall dynamic range achieved for GIXD as presented in Fig. 10 is approximately five orders of magnitude. This range is not limited by the noise of the detector or the overall scattering background, but it is inherently determined by the intensity distribution of diffuse scattering from the QDs.

6. Discussion

The following items highlight the particular advantages offered by our experimental set-up for grazing-incidence X-ray diffraction.

(i) First, as the main advantage of our set-up, three-dimensional mapping of reciprocal space can be performed by a single scan, for example, a rocking scan (ω scan) of the sample. Since only a single scan is needed, the data collection time is significantly reduced to typically a few hours only.

(ii) The loss of scattered intensity caused by the use of a small detector slit s_2 is overcompensated by the employment of a two-dimensional detector (multi-detection). In addition, the CCD detector exhibits a higher dynamic range as compared with conventional wire detectors where the intensity per pixel is restricted to typically a few 1000 counts s^{-1} channel^{-1}.

(iii) The in-plane angular resolution $\delta(2\theta)$ and in-plane angular range $\Delta(2\theta)$ are tunable and can be adapted to the requirements of a particular sample.

(iv) The in-plane angular resolution $\delta(2\theta)$ does not depend on the horizontal beam size p_2. Therefore, the slit p_2 can be opened as much as possible in order to obtain maximum photon flux on the sample.

(v) The angular range $\Delta(2\theta)$ scales with $\sin(2\theta)$. On the other hand, the radial extension of diffuse scattering often scales with $\sin(2\theta)$. Consequently, the experimental set-up need not be modified if a set of different in-plane reflections are under investigation.

(vi) Typical values for the in-plane angular resolution and in-plane angular range are $\delta(2\theta) = 0.013°$ and $\Delta(2\theta) = 4°$ which perfectly fit to the requirements given by strained nanostructures. For example, Ge nano-islands grown on Si substrates exhibit a lattice mismatch of 4.2% leading to a maximum angular range of about $\Delta(2\theta) = 2°$ for the 022 reflection at $\lambda = 1.5$ Å.

Compared with these items, there are only some minor restrictions.

(i) In the geometry shown in Fig. 5, different in-plane scattering angles 2θ

correspond to different scattering origins on the sample. In special cases where the sample is (intentionally) laterally inhomogeneous this interrelation between scattering angle 2θ and location on the sample could represent an undesirable fact. However, also the standard triple-crystal geometry, using a single crystal for analyzing the scattering angle 2θ, is influenced by lateral inhomogeneities of the sample. Here an average over these inhomogeneities is taken which leads to peak broadening in the 2θ direction.

(ii) The typical in-plane angular resolution of our set-up $[\delta(2\theta) = 0.013°]$ is about one order of magnitude worse as compared with a triple-crystal set-up using a Si(111) crystal analyzer $[\Delta(2\theta)_{\mathrm{TRIPLE}} = 0.002°]$. This very high resolution is, however, often not necessary for the investigation of mesoscopic structures.

7. Conclusion

To conclude, we have presented a novel method where a CCD detector is used in order to three-dimensionally probe the X-ray diffuse scattering in the vicinity of an in-plane reciprocal lattice point. Since only a single rocking scan of the sample is performed, the total data acquisition time is strongly reduced as compared with a classical triple-crystal set-up. Although angular resolution and angular range are tunable, our set-up is particularly suited for the investigation of small strained objects where ultra-high resolution is not needed and the intensity is widely spread in reciprocal space.

References

Bimberg, D., Grundmann, M. & Ledentsov, N. N. (1998). *Quantum Dot Heterostructures.* Chichester: Wiley.

Feidenhans'l, R. (1989). *Surface Sci. Rep.* **10**, 105–188.

Fontaine, P., Goldmann, M., Bordessoule, M. & Jucha, A. (2004). *Rev. Sci. Instrum.* **75**, 3097–3106.

Foran, G. J., Peng, J. B., Steitz, R., Barnes, G. T. & Gentle, I. R. (1996). *Langmuir,* **12**, 774–777.

Kegel, I., Metzger, T. H., Lorke, A., Peisl, J., Stangl, J., Bauer, G., Garcia, J. M. & Petroff, P. M. (2000). *Phys. Rev. Lett.* **85**, 1694–1697.

Kegel, I., Metzger, T. H., Peisl, J., Stangl, J., Bauer, G. & Smilgies, D. (1999). *Phys. Rev. B,* **60**, 2516–2521.

Lee, S. R., Doyle, B. L., Drummond, T. J., Medernach, J. W. & Schneider, R. P. (1995). *Adv. X-ray Anal.* **38**, 201.

Levine, J. R., Cohen, J. B., Chung, Y. W. & Georgopoulos, P. (1989). *J. Appl. Cryst.* **22**, 528–532.

Mathieson, A. McL. (1982). *Acta Cryst.* A**38**, 378–387.

Naudon, A. & Thiaudiere, D. (1997). *J. Appl. Cryst.* **30**, 822–827.

Pietsch, U., Holý, V. & Baumbach, T. (2004). *High-Resolution X-ray Scattering – From Thin Films to Lateral Nanostructures.* Berlin: Springer.

Schlepütz, C. M., Herger, R., Willmott, P. R., Patterson, B. D., Bunk, O., Brönnimann, Ch., Henrich, B., Hülsen, G. & Eikenberry, E. F. (2005). *Acta Cryst.* A**61**, 418–425.

Schmidbauer, M. (2004). *Springer Tracts in Modern Physics,* Vol. 199, *X-ray Diffuse Scattering From Self-Organized Mesoscopic Semiconductor Structures.* Berlin: Springer.

Schmidbauer, M., Grigoriev, D., Hanke, M., Schäfer, P., Wiebach, T. & Köhler, R. (2005). *Phys. Rev. B,* **71**, 115324.

Schmidbauer, M., Seydmohamadi, Sh., Grigoriev, D., Wang, Zh. M., Mazur, Yu. I., Schäfer, P., Hanke, M., Köhler, R. & Salamo, G. J. (2006). *Phys. Rev. Lett.* **96**, 066108.

Schmidbauer, M., Wiebach, T., Raidt, H., Hanke, M., Köhler, R. & Wawra, H. (1998). *Phys. Rev. B,* **58**, 10523–10531.

Shchukin, V. A., Ledentsov, N. N. & Bimberg, D. (2003). *Epitaxy of Nanostructures.* Berlin: Springer.

Springholz, G., Holý, V., Pinczolits, M. & Bauer, G. (1998). *Science,* **282**, 734–737.

Stangl, J., Holý, V. & Bauer, G. (2004). *Rev. Mod. Phys.* **76**, 725–783.

Stangl, J., Roch, T., Holý, V., Pinczolits, M., Springholz, G., Bauer, G., Kegel, I., Metzger, T. H., Zhu, J., Brunner, K., Abstreiter, G. & Smilgies, D. (2000). *J. Vac. Sci. Technol. B,* **18**, 2187–2192.